Control of Coherently Coupled Exciton Polaritons in Monolayer Tungsten Disulphide

Xiaoze Liu,[1] Wei Bao,[1] Quanwei Li,[1] Chad Ropp,[1] Yuan Wang,[1,2] and Xiang Zhang[1,2,*]
[1]NSF Nanoscale Science and Engineering Center, University of California, Berkeley, California 94720, USA
[2]Materials Sciences Division, Lawrence Berkeley National Laboratory, Berkeley, California 94720, USA
(Received 15 November 2016; published 14 July 2017)

Monolayer transition metal dichalcogenides (TMD) with confined 2D Wannier-Mott excitons are intriguing for the fundamental study of strong light-matter interactions and the exploration of exciton polaritons at high temperatures. However, the research of 2D exciton polaritons has been hindered because the polaritons in these atomically thin semiconductors discovered so far can hardly support strong nonlinear interactions and quantum coherence due to uncontrollable polariton dynamics and weakened coherent coupling. In this work, we demonstrate, for the first time, a precisely controlled hybrid composition with angular dependence and dispersion-correlated polariton emission by tuning the polariton dispersion in TMD over a broad temperature range of 110–230 K in a single cavity. This tamed polariton emission is achieved by the realization of robust coherent exciton-photon coupling in monolayer tungsten disulphide (WS_2) with large splitting-to-linewidth ratios (>3.3). The unprecedented ability to manipulate the dispersion and correlated properties of TMD exciton polaritons at will offers new possibilities to explore important quantum phenomena such as inversionless lasing, Bose-Einstein condensation, and superfluidity.

DOI: 10.1103/PhysRevLett.119.027403

Two-dimensional (2D) semiconducting transition metal dichalcogenides (TMD) have been an attractive group of semiconductors since the discovery of the transition from indirect to direct band gap at the monolayer limit [1–3]. Because of their quantum confinement at reduced dimensionality and crystal symmetry, the TMD monolayers have very large exciton binding energies up to ~0.7 eV [4–6], huge oscillator strengths [1,7], and a valley degree of freedom [8–11]. These exceptional properties bolster the formation of exciton polaritons in optical cavities [12–19] with a great potential for applications in quantum information, communication, and computing. In semiconductor microcavities (MC), the part-light part-matter polaritons are formed in the strong coupling regime where the coupling rate is faster than the average dissipation rates of light and matter. When a distinct polariton energy dispersion is present, these bosonic quasiparticles can follow the Bose-Einstein statistics with small effective masses, enabling Bose-Einstein condensation (BEC) at elevated temperatures [20–22].

The realization of polariton condensation at higher temperatures requires excitons that are robust to thermal fluctuations, coherent coupling between the exciton and photon that are maintained under high polariton densities, and polariton dynamics that are optimized through a well-balanced hybrid composition within a distinct energy dispersion (such as the angular dependent energy diagram). In this context, TMD monolayers that provide delocalized (Wannier-Mott) excitons with large binding energies and a distinct valley degree of freedom [12,23], are a unique semiconductor system for room temperature polariton condensation with optical spin degrees of freedom. However, the research of TMD exciton polaritons has been hindered by (i) the weakened coherent coupling, indicated by small splitting-to-linewidth ratios (SLR), and (ii) uncontrolled and extremely fast polariton dynamics. The coherent coupling is represented by SLR, i.e., the average number of energy oscillations between excitons and photons during the polariton lifetime [24] (see the Supplemental Material [25] for more details). More importantly, to maintain unperturbed coherent coupling at high pump density, support strong nonlinear polariton interactions, and slow down the polariton leakage rate with respect to the nonlinear interaction rate, a large SLR is essential for polariton condensation [24]. After the first demonstration of exciton polaritons in a MoS_2 monolayer-based MC [12], various approaches [13–18] have been employed for further polariton study, but with limitations on reduced Rabi splitting, low temperature operation (<20 K), and small SLR (typically <2). These limitations prevent coherent strong coupling at high pump injection, which is the key for room temperature polariton condensation. On the other hand, polariton condensation strongly depends on the optimized dynamics via the well-balanced hybrid composition in the energy dispersion diagram, which holds only when the exciton component has a significantly slower decay rate than the photon leakage rate. Yet, the TMD exciton decay process, involving defect-mediated nonradiative recombination [29], trion [30,31], and dark exciton [32] quenching at low temperatures, is ultrafast (typically <10 ps) and comparable with the photon leakage lifetime. Hence, the optimized polariton dynamics in TMD has not been demonstrated. In this work, we show that the angular dependent hybrid composition with a full dispersion is, for the first time, controlled by directly tuning the TMD

exciton energy over a broad temperature range (110–230 K), where coherently coupled TMD exciton polaritons with a large SLR > 3.3 are sustained. Because of the enhanced long exciton lifetime (>200 ps), the angular dependent intensity distribution of polariton PL reveals a clear correlation with the hybrid composition of excitons and photons as a function of temperature. This correlation provides a distinctive basis for control of polariton dynamics by tuning of the hybrid composition in a single cavity device, which is in contrast to the requirement that samples be varied in conventional semiconductor systems to span polariton configurations [22,33–37]. Our findings demonstrate an ideal platform for manipulating the TMD polaritons at will and open the door towards realization of 2D polariton condensation at room temperature.

To achieve a large SLR for strongly coupled exciton polaritons, we introduce an efficient strategy to incorporate monolayer tungsten disulphide (WS_2) into a compact all-dielectric MC. Coherent coupling with a larger SLR requires a small cavity length to increase Rabi splitting, and a larger quality factor to reduce polariton linewidth. The cavity structure is shown in the schematic of Fig. 1(a), where the bottom mirror is 12.5 pairs of a SiO_2/Si_3N_4 distributed Bragg reflector (DBR) while the top mirror is 7.5 pairs of a SiO_2/Si_3N_4 DBR. Since the monolayer WS_2 exciton is fragile to the fabrication process [3,29,38], we utilize hydrogen silsesquioxane (HSQ) to form a sandwich structure around the exfoliated monolayer WS_2 (HQ Graphene, Inc.) that preserves the electronic and optical quality of TMD monolayers [39,40]. An Al_2O_3 layer is grown on top of capping HSQ to further protect the WS_2 layer from the high temperature plasma during growth of the top DBR. The monolayer area is shown in the microscopic image of the Fig. 1(b) inset. The HSQ thickness is controlled to achieve a MC cavity resonance at 2.052 eV for normal incidence (the in-plane wave number $k_{\|} = 0$), determined by the reflectivity (see Ref. [25], Fig. S1). The cavity resonance needs to overlap with the exciton energy over a broad temperature range with only negligible influences from the trions and dark excitons in order to demonstrate the clear feature of the coherently coupled exciton polariton and the control of polariton dispersion as a function of detuning (determined by temperature). Based on the normal cavity resonance E_{ph} at 2.052 eV, the cavity shows angular dependence of $E_{cav}(\theta) = E_{ph}/\sqrt{1-[\sin(\theta)/n_{eff}]^2}$ as in Fig. S1(a) [25]. Moreover, at the normal incidence the total quality factor of the MC is measured to be ~400, corresponding to a cavity full width at half maximum (FWHM) of ~5 meV. Our strategy thus ensures the excitonic performance of WS_2 is boosted without sacrificing the cavity quality factor or expanding the cavity length.

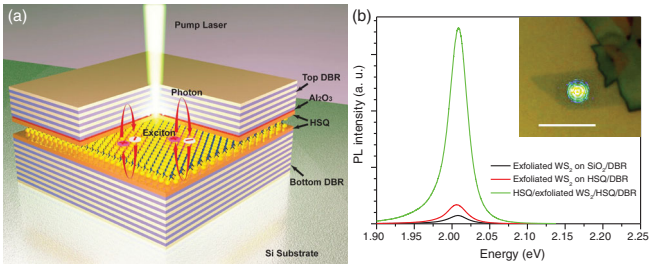

FIG. 1. Schematic of TMD microcavity and improved WS_2 exciton emission. (a) Schematic of the microcavity (MC) structure. It consists of 12.5 periods of a SiO_2/Si_3N_4 bottom distributed DBR and 7.5 periods of a top DBR. The cavity layer structure includes an exfoliated monolayer WS_2 flake sandwiched by two HSQ layers. There is a thin Al_2O_3 film atop of the top HSQ layer to protect the WS_2 during the top DBR growth. (b) The WS_2 photoluminescence spectra of exfoliated WS_2 on SiO_2/DBR and HSQ/DBR substrates, and WS_2 on HSQ/DBR capped with HSQ and Al_2O_3 layer under the same pump and collection conditions. Besides the intensity enhancement, the PL peak position and FWHM are all consistent. The inset shows the optical image of the monolayer WS_2 flake (the light-green trapezoid shape) with a laser beam at the center (the white circular shape) before depositing the top DBR, the scale bar corresponds to 10 μm.

The exciton linewidth and decay process can not only affect the coherent coupling, but also modify the polariton dynamics. The excitonic performance can be characterized by the exciton PL measurements. PL spectra of the WS_2 monolayer measured with different substrates and capping conditions [Fig. 1(b)], along with time-resolved PL of WS_2 on HSQ (Fig. S2), confirm that HSQ enhances the excitonic performance. Compared with the PL spectra of WS_2 on substrates of SiO_2/DBR and on HSQ/DBR, the PL of WS_2 sandwiched by two HSQ layers shows a peak intensity that is increased by a factor of >10 and a lifetime ~220 ps at low pump fluence, corresponding to a PL quantum efficiency of ~10%. Moreover, the PL spectra all show a consistent dominant excitonic peak at ~2.006 eV with FWHM of ~30 meV. Note here that the observed PL quantum efficiency is still within the optical linear regime and stays unchanged up to a pump fluence of 0.1 $\mu J/cm^2$ (Fig. S2), different from the reported chemically treated monolayer MoS_2 [29], whose high quantum efficiency becomes suppressed at pump fluences >0.01 $\mu J/cm^2$ due to the Auger recombination. With the HSQ capping layers, the WS_2 excitons preserve their apparent temperature-dependent shift (from 2.006 eV around 295 K to 2.085 eV around 10 K) as shown in Fig. S3, distinct from other temperature-insensitive cases [41,42]. Because of the emergence of trions [30] and dark excitons [32] at low temperature, our MC sample is only studied at temperatures >110 K, where the exciton peak dominates.

We reach the strong coupling regime by first cooling down the MC to 110 K where the cavity detuning is $\Delta = E_{ph} - E_{ex} = -26$ meV. The k-space (angle-resolved) reflectivity is then characterized using white light as shown

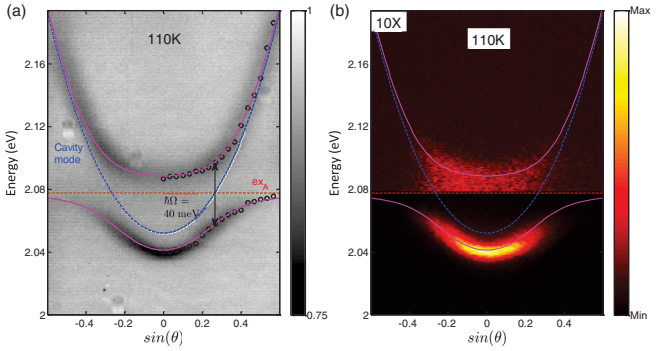

FIG. 2. k-space reflectivity and photoluminescence at 110 K. (a) The reflectivity map at 110 K obtained by k-space spectroscopy, where the horizontal axis represents the sine function of the incidence angles (θ) and the vertical axis is the photon energy. The gray color scale represents the reflectivity with darker areas corresponding to lower reflectivity. Two reflectivity modes are identified as the two anti-crossing polariton branches with dispersion fitted by a coupled oscillator model [25] with a 40 meV Rabi splitting. The dispersion plot is overlaid with the reflectivity map, with the dashed red line representing the exciton energy (2.078 eV), the dashed blue curve as the cavity photon dispersion, and the two solid magenta curves are the fitted polariton dispersion. This coupled oscillator model shows excellent agreement with the experimental reflectivity. (b) The nonresonantly pumped PL map obtained by k-space spectroscopy at 110 K. The orange color scale represents the PL intensity. The intensity of the upper polariton PL is magnified by 10× due to its weak emission. The reflectivity dispersion is directly translated here and shows excellent agreement with the PL dispersion.

in Fig. 2(a). More details of the k-space characterization is discussed in the Supplemental Material and Fig. S4 [25], and the data shown here are based on TM polarization unless otherwise noted. Two reflectivity modes appear with the higher-energy mode's dispersion flattened at small incidence angles and the lower-energy mode's dispersion flattened at larger angles. This is a typical signature of a two-branch polariton dispersion, indicating that the system is in the strong coupling regime. Note here the polariton states are the superposition of the original cavity mode and exciton resonance, so they show a very distinct angular dependence with apparently anticrossed branches from the original cavity dispersion (Fig. S1) and flat exciton dispersion (Fig. S5). The cavity photon dispersion is shown as the blue dashed curve while the exciton energy, at 2.078 eV, is shown as the red dashed line, which is based on the temperature-dependent PL (Fig. S3). The FWHM of the polariton branches (identified by the magenta curves) are both less than 12 meV, with the Rabi splitting read directly as ~40 meV at $\sin(\theta)$ of 0.25, yielding a high SLR > 3.3. This large SLR is clear from the splitting feature without peak fitting, demonstrating sufficient round-trip energy oscillations during the exciton-photon coupling and thus obvious coherent coupling.

This Rabi splitting is consistent with a coupled oscillator model as

$$\begin{pmatrix} E_{\mathrm{ex}} + i\hbar\Gamma_{\mathrm{ex}} & V_A \\ V_A & E_{\mathrm{cav}}(\theta) + i\hbar\Gamma_{\mathrm{cav}} \end{pmatrix} \begin{pmatrix} \alpha \\ \beta \end{pmatrix} = E \begin{pmatrix} \alpha \\ \beta \end{pmatrix}. \quad (1)$$

E_{ex} and E_{cav} are the exciton and cavity photon energies, respectively. And the Γ_{cav} and Γ_{ex} are the half width at half maximum (HWHM) of the cavity photon and exciton, respectively. E are the eigenvalues corresponding to the energies of polariton modes. α and β construct the eigenvectors where $|\alpha|^2 + |\beta|^2 = 1$. V_A is the coupling strength. This leads to the eigenvalues $E = [(E_{\mathrm{ex}} + E_{\mathrm{cav}})/2] + i[(\hbar\Gamma_{\mathrm{ex}} + \hbar\Gamma_{\mathrm{cav}})/2] \pm \sqrt{V_A^2 + \frac{1}{4}(E_{\mathrm{ex}} - E_{\mathrm{cav}} + i\hbar\Gamma_{\mathrm{ex}} - i\hbar\Gamma_{\mathrm{cav}})^2}$ where the Rabi splitting $\hbar\Omega_{\mathrm{Rabi}} = 2\sqrt{V_A^2 - \frac{1}{4}(\hbar\Gamma_{\mathrm{ex}} - \hbar\Gamma_{\mathrm{cav}})^2}$ at detuning $\Delta = E_{\mathrm{cav}} - E_{\mathrm{ex}} = 0$. More details of this model are also elaborated in the Supplemental Material [25].

To fit this model with the data, the reflectivity minima are extracted from the k-space reflectivity and the calculated polariton dispersion is obtained, which overlays exactly with the data. Specifically, at zero detuning where the polariton linewidth is around 12 meV, the difference of HWHM between excitons and cavity photons is estimated to be ~7 meV, the Rabi splitting of 40 meV yields a coupling strength V_A of 20.3 meV.

To show how the polariton states are populated by scattering and thermal relaxation from the nonresonantly pumped exciton reservoir, the MC is nonresonantly pumped by a pulsed laser with a wavelength of 510 nm, which lies just outside the reflectivity stop band of the MC (see the Supplemental Material [25] for PL measurement details). In Fig. 2(b), the k-space PL map shows a dominant lower polariton (LP) PL intensity with a maximum peak at the lowest polariton state. The upper polariton (UP) intensity is much weaker than the LP, so the PL intensity at the higher photon energy panel is magnified by 10 times to be visible in the figure. The dispersion plot overlaid with this PL map is directly translated from the reflectivity dispersion without any fitting. As clearly shown, the dispersion curves are very consistent with the PL distribution, confirming that the polariton states are stable after the scattering and thermal relaxation in this nonresonantly pumped process. Moreover, the large contrast of PL intensity between the UP and LP states indicates a more photonlike LP, with faster decay rate, as well as the most photonlike LP state (lowest LP state) with fastest rate, uncovering a hybrid composition-determined polariton dynamics.

If the polariton decay rate is slower than the polariton relaxation process, it can be determined by the exciton and photon rates with weighing fraction (i.e., Hopefield coefficient, see Supplemental Material [25]), varying along the dispersion as

$$\gamma_{LP} = |\alpha|^2\gamma_{ex} + |\beta|^2\gamma_{cav}$$
$$\gamma_{UP} = |\beta|^2\gamma_{ex} + |\alpha|^2\gamma_{cav}, \quad (2)$$

where $|\alpha|^2$, $|\beta|^2$ represent weighing fractions of the exciton and cavity photon, respectively;γ_{LP}, γ_{UP} refer to the decay rates of the LP and UP states, respectively; γ_{ex}, γ_{cav} represent the decay rates of the exciton (lifetime ~200 ps, Fig. S2 [25]) and cavity photon (lifetime ~1 ps), respectively. Because of the much faster cavity decay rate, polaritons with larger photon fraction will decay faster, resulting in a varying emission intensity distribution that depends on the hybrid composition.

The exciton-polariton composition, as a vital physical quantity for controlling the nonlinear interactions in polariton condensates [35,43], can be directly managed through cavity-excition detuning ($\Delta = E_{ph} - E_{ex}$, see the Supplemental Material [25]). This detuning is most often achieved through cumbersome modification of the photon part [22,33–37] due to the difficulty in controlling the exciton part. However, TMD monolayers have Wannier-Mott excitons with large binding energies [4] that enable the tuning of the exciton part over a large temperature range. This strong temperature dependence is extremely difficult to achieve with other material systems because of the weak exciton binding energies in the conventional quantum well systems, the multiexciton convolutions in wide-band-gap semiconductors, as well as the temperature insensitivity of Frenkel excitons in organic materials. Here we demonstrate, for the first time, the tuning of the exciton part of the polariton as a function of temperature to control the cavity detuning in a single MC sample. The sample temperature is set to be 130, 210, and 230 K, corresponding to the detuning of −20, 2, and 10 meV, respectively. In Fig. 3(a), the exciton dashed line redshifts as the temperature increases while the cavity resonance stays almost the same, creating the crossing and noncrossing features in the exciton and original cavity dispersion. The polariton branches, though modified significantly due to the various cavity detunings, are both unambiguously identified based on the anticrossing reflectivity modes. Using the same model with corresponding exciton energies, the Rabi splittings are fitted to be 39 meV ($V_A = 19.8$ meV) at 130 K, 37 meV ($V_A = 18.8$ meV) at 210 K, and 36 meV ($V_A = 18.3$ meV) at 230 K, which are consistent across all these temperatures. The k-space PL at these temperatures is also shown in Fig. 3(b), where the overlaid reflectivity dispersions agree well with the PL intensity distribution. The UP intensity is still magnified to be comparable with the LP intensity, indicating that the LP states are similarly stable over a large temperature range. Note that the magnifications of the upper panels become smaller as temperature increases, due to the significant change in the polariton composition.

The polariton composition from the exciton and photon can be characterized by the weighing fractions, calculated as the Hopfield coefficients as a function of cavity detunings [25]. The Hopfield coefficients for the LP branch are plotted in Fig. 4 for various temperatures. With the large binding energy and strong temperature dependence, the excitons are robust and tunable over a much broader temperature range. As the cavity detuning changes from negative (130 K), to near zero (210 K), to positive (230 K), the Hopfield coefficients show that the LPs can be flexibly tuned from a more photonlike, to a photon-exciton-mixed, and to a more excitonlike state at small incidence angles. This tunability provides the freedom to control the

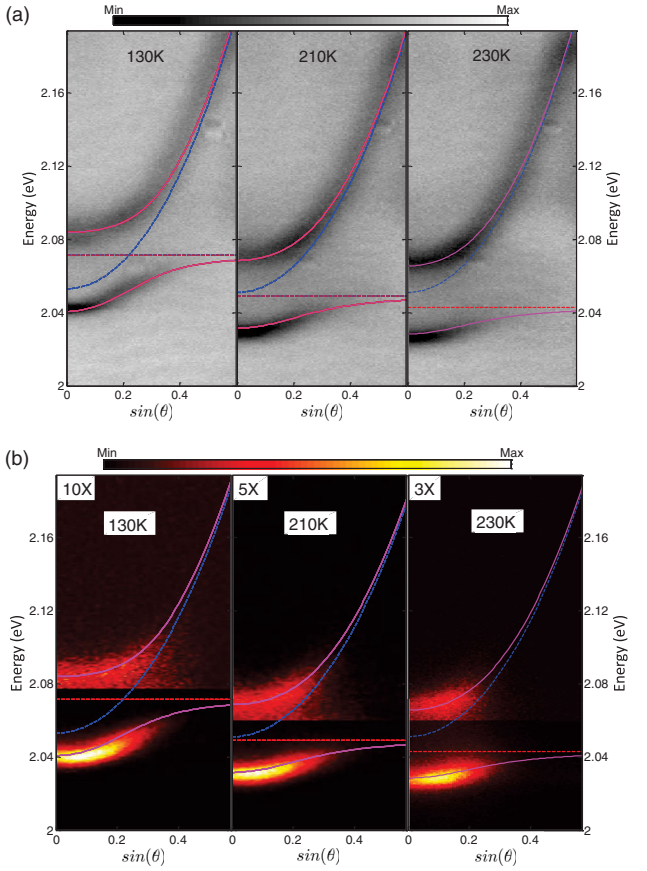

FIG. 3. Temperature-dependent reflectivity and PL. (a) The k-space reflectivity map at temperatures of 130, 210, and 230 K. As the temperature increases, the exciton (the red dashed line) red shifts from 2.072 to 2.042 eV, while the cavity photon dispersion (the blue dashed curve) does not change, creating various cavity detunings over this temperature range. The coupled oscillator model is calculated to fit the dispersions (magenta solid curves) showing that the strong coupling regime holds at all these temperatures with large splitting-to-linewidth ratio. (b) The k-space PL map at temperatures of 130, 210, and 230 K. The reflectivity dispersions are directly translated here showing the agreement between the reflectivity and PL dispersions. Since the UP PL is much weaker, the intensity is still magnified by 10×, 5×, and 3× at the upper panels at all these temperatures, respectively. Note here that the UP PL intensity becomes comparable with LP intensity as the UP becomes more photonlike at higher temperatures.

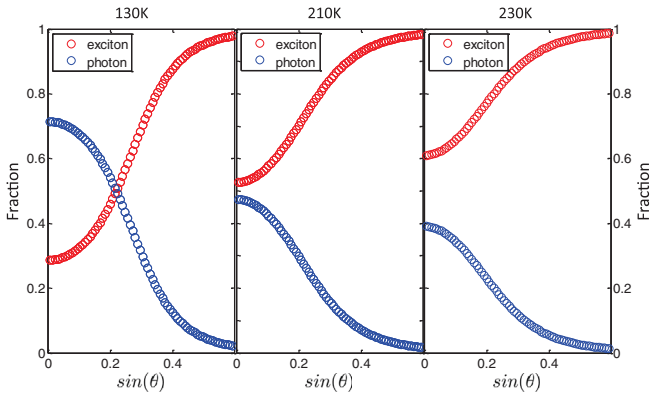

FIG. 4. Hopfield coefficients of lower polariton states at three temperatures. Based on the coupled oscillator model, the contributions from exciton and photon components on the polariton states can be characterized by Hopfield coefficients [25]. The Hopfield coefficients given as a function of the incidence angle indicate how the polaritons are hybridized by the excitons and photons. As temperature increases, the cavity detuning changes from negative to positive, leading to a transition from a more photonlike to a more excitonlike state. This transition also alters the emission dynamics of the polaritons and thus the PL intensity distribution as seen in Fig. 3(b).

polariton composition at will, and thus to optimize the polariton dynamics.

The polariton composition reveals clear correlation with the PL intensity distribution at different temperatures as shown in Fig. 3(b). At negative detuning, the LP is more photonlike at small angles, while becoming more excitonlike at large angles. Since the WS_2 exciton lifetime of ~200 ps is much longer than the cavity photon leakage lifetime of ~1 ps, the more photonlike polariton (LP branch) lifetime is generally smaller than the more excitonlike polariton (UP branch) lifetime. The LP states have a faster lifetime, and are thus the preferred states for polariton leakage emission, which is consistent with PL intensity of the LP state being maximal throughout all temperatures 110–230 K. Once the detuning becomes positive, at small angle the LP starts to become more excitonlike while the UP becomes more photonlike. The photonlike trend of the UP branch at positive detuning decreases the UP leakage lifetime, enhancing the UP PL intensity. This transition of the hybrid polariton composition leads to less emission contrast between the UP and LP states at higher temperatures.

In summary, the unambiguous control of polariton dispersion is demonstrated in a WS_2 MC, due to the large exciton binding energy, strong temperature dependence of Wannier excitons, unperturbed exciton quantum yield, and lifetime over a large temperature range. By tuning the polariton dispersion, the angular dependent polariton composition can be flexibly controlled, enabling the control of polariton emission dynamics. This controllability illustrates a powerful way to optimize polariton dynamics and paves the way to realize polariton condensation in TMD monolayers. Furthermore, the coherent strong coupling with a large SLR of 3.3 not only ensures the fundamental basis for polariton condensation, but also holds great promise to preserve the coherence of valley excitons in TMD monolayers.

This work is supported by Office of Naval Research (ONR) Multidisciplinary University Research Initiative (MURI) program under Grant No. N00014-13-1-0649, and National Science Foundation (EFMA-1542741).

X. L. and W. B. contributed equally to this work.

*xiang@berkeley.edu

[1] K. F. Mak, C. Lee, J. Hone, J. Shan, and T. F. Heinz, Phys. Rev. Lett. **105**, 136805 (2010).
[2] A. Splendiani, L. Sun, Y. Zhang, T. Li, J. Kim, C.-Y. Chim, G. Galli, and F. Wang, Nano Lett. **10**, 1271 (2010).
[3] Q. H. Wang, K. Kalantar-Zadeh, A. Kis, J. N. Coleman, and M. S. Strano, Nat. Nanotechnol. **7**, 699 (2012).
[4] Z. Ye, T. Cao, K. O'Brien, H. Zhu, X. Yin, Y. Wang, S. G. Louie, and X. Zhang, Nature (London) **513**, 214 (2014).
[5] A. Chernikov, T. C. Berkelbach, H. M. Hill, A. Rigosi, Y. Li, O. B. Aslan, D. R. Reichman, M. S. Hybertsen, and T. F. Heinz, Phys. Rev. Lett. **113**, 076802 (2014).
[6] K. He, N. Kumar, L. Zhao, Z. Wang, K. F. Mak, H. Zhao, and J. Shan, Phys. Rev. Lett. **113**, 026803 (2014).
[7] Y. Li, A. Chernikov, X. Zhang, A. Rigosi, H. M. Hill, A. M. van der Zande, D. a. Chenet, E.-M. Shih, J. Hone, and T. F. Heinz, Phys. Rev. B **90**, 205422 (2014).
[8] T. Cao, G. Wang, W. Han, H. Ye, C. Zhu, J. Shi, Q. Niu, P. Tan, E. Wang, B. Liu, and J. Feng, Nat. Commun. **3**, 887 (2012).
[9] H. Zeng, J. Dai, W. Yao, D. Xiao, and X. Cui, Nat. Nanotechnol. **7**, 490 (2012).
[10] K. F. Mak, K. He, J. Shan, and T. F. Heinz, Nat. Nanotechnol. **7**, 494 (2012).
[11] G. Wang, X. Marie, B. L. Liu, T. Amand, C. Robert, F. Cadiz, P. Renucci, and B. Urbaszek, Phys. Rev. Lett. **117**, 187401 (2016).
[12] X. Liu, T. Galfsky, Z. Sun, F. Xia, E. Lin, Y.-H. Lee, S. Kéna-Cohen, and V. M. Menon, Nat. Photonics **9**, 30 (2015).
[13] S. Dufferwiel, S. Schwarz, F. Withers, A. A. P. Trichet, F. Li, M. Sich, O. Del Pozo-Zamudio, C. Clark, A. Nalitov, D. D. Solnyshkov, G. Malpuech, K. S. Novoselov, J. M. Smith, M. S. Skolnick, D. N. Krizhanovskii, and A. I. Tartakovskii, Nat. Commun. **6**, 8579 (2015).
[14] M. Sidler, P. Back, O. Cotlet, A. Srivastava, T. Fink, M. Kroner, E. Demler, and A. Imamoglu, arXiv: 1603.09215.
[15] S. Wang, S. Li, T. Chervy, A. Shalabney, and S. Azzini, Nano Lett. **16**, 4368 (2016).
[16] T. Hu, Y. Wang, L. Wu, L. Zhang, Y. Shan, J. Lu, J. Wang, S. Luo, Z. Zhang, L. Liao, S. Wu, S. C. Shen, and Z. Chen, arXiv 1606.05838v1.
[17] L. C. Flatten, Z. He, D. M. Coles, A. A. P. Trichet, A. W. Powell, R. A. Taylor, J. H. Warner, and J. M. Smith, arXiv 1605.04743.

[18] N. Lundt, S. Klembt, E. Cherotchenko, O. Iff, A. V. Nalitov, M. Klaas, S. Betzold, C. P. Dietrich, A. V. Kavokin, S. Höfling, and C. Schneider, arXiv 1604.03916.
[19] W. Zhao, S. Wang, B. Liu, I. Verzhbitskiy, S. Li, F. Giustiniano, D. Kozawa, K. P. Loh, K. Matsuda, K. Okamoto, R. F. Oulton, and G. Eda, Adv. Mater. **28**, 2709 (2016).
[20] T. Byrnes, N. Y. Kim, and Y. Yamamoto, Nat. Phys. **10**, 803 (2014).
[21] H. Deng and Y. Yamamoto, Rev. Mod. Phys. **82**, 1489 (2010).
[22] J. Kasprzak, M. Richard, S. Kundermann, A. Baas, P. Jeambrun, J. M. J. Keeling, F. M. Marchetti, M. H. Szymańska, R. André, J. L. Staehli, V. Savona, P. B. Littlewood, B. Deveaud, and L. S. Dang, Nature (London) **443**, 409 (2006).
[23] K. F. Mak and J. Shan, Nat. Photonics **10**, 216 (2016).
[24] G. Khitrova and H. M. Gibbs, Rev. Mod. Phys. **71**, 1591 (1999).
[25] See Supplemental Material at http://link.aps.org/supplemental/10.1103/PhysRevLett.119.027403 for experimental details, modeling, and supplementary figures. It also includes Refs. [26–28].
[26] V. Savona, L. C. Andreani, P. Schwendimann, and A. Quattropani, Solid State Commun. **93**, 733 (1995).
[27] N. Kumar, Q. Cui, F. Ceballos, D. He, Y. Wang, and H. Zhao, Phys. Rev. B **89**, 125427 (2014).
[28] S. Mouri, Y. Miyauchi, M. Toh, W. Zhao, G. Eda, and K. Matsuda, Phys. Rev. B **90**, 155449 (2014).
[29] M. Amani, D.-H. Lien, D. Kiriya, J. Xiao, A. Azcatl, J. Noh, S. R. Madhvapathy, R. Addou, S. KC, M. Dubey, K. Cho, R. M. Wallace, S.-C. Lee, J.-H. He, J. W. Ager, X. Zhang, E. Yablonovitch, and A. Javey, Science **350**, 1065 (2015).
[30] K. F. Mak, K. He, C. Lee, G. H. Lee, J. Hone, T. F. Heinz, and J. Shan, Nat. Mater. **12**, 207 (2013).
[31] A. Singh, G. Moody, S. Wu, Y. Wu, N. J. Ghimire, J. Yan, D. G. Mandrus, X. Xu, and X. Li, Phys. Rev. Lett. **112**, 216804 (2014).
[32] X.-X. Zhang, Y. You, S. Y. F. Zhao, and T. F. Heinz, Phys. Rev. Lett. **115**, 257403 (2015).
[33] H. Deng, G. Weihs, C. Santori, J. Bloch, and Y. Yamamoto, Science **298**, 199 (2002).
[34] S. Christopoulos, G. von Högersthal, A. Grundy, P. Lagoudakis, A. Kavokin, J. Baumberg, G. Christmann, R. Butté, E. Feltin, J.-F. Carlin, and N. Grandjean, Phys. Rev. Lett. **98**, 126405 (2007).
[35] F. Li, L. Orosz, O. Kamoun, S. Bouchoule, C. Brimont, P. Disseix, T. Guillet, X. Lafosse, M. Leroux, J. Leymarie, M. Mexis, M. Mihailovic, G. Patriarche, F. Réveret, D. Solnyshkov, J. Zuniga-Perez, and G. Malpuech, Phys. Rev. Lett. **110**, 196406 (2013).
[36] K. Daskalakis, S. Maier, R. Murray, and S. Kéna-Cohen, Nat. Mater. **13**, 271 (2014).
[37] J. D. Plumhof, T. Stoeferle, L. Mai, U. Scherf, and R. Mahrt, Nat. Mater. **13**, 247 (2014).
[38] M. Chhowalla, H. S. Shin, G. Eda, L.-J. Li, K. P. Loh, and H. Zhang, Nat. Chem. **5**, 263 (2013).
[39] H. Zhu, Y. Wang, J. Xiao, M. Liu, S. Xiong, Z. J. Wong, Z. Ye, and Y. Ye, Nat. Nanotechnol. **10**, 151 (2015).
[40] Y. Ye, Z. J. Wong, X. Lu, X. Ni, H. Zhu, X. Chen, Y. Wang, and X. Zhang, Nat. Photonics **9**, 733 (2015).
[41] G. Plechinger, F.-X. Schrettenbrunner, J. Eroms, D. Weiss, C. Schüller, and T. Korn, Phys. Status Solidi—Rapid Res. Lett. **6**, 126 (2012).
[42] D. Yoon, Y. Son, and H. Cheong, Nano Lett. **11**, 3227 (2011).
[43] O. Jamadi, F. Réveret, E. Mallet, P. Disseix, F. Médard, M. Mihailovic, D. Solnyshkov, G. Malpuech, J. Leymarie, X. Lafosse, S. Bouchoule, F. Li, M. Leroux, F. Semond, and J. Zuniga-Perez, Phys. Rev. B **93**, 115205 (2016).